JVST B
Journal of Vacuum Science & Technology B

ARTICLE

pubs.aip.org/avs/jvb

Plasma-assisted annealing of Pt-doped rutile TiO_2 nanoparticles for enhanced decomposition and bacterial inactivation under general lighting

Cite as: J. Vac. Sci. Technol. B **42**, 012203 (2024); doi: 10.1116/6.0003101
Submitted: 30 August 2023 · Accepted: 19 December 2023 ·
Published Online: 11 January 2024

Retsuo Kawakami,[1,a] Yuta Makino,[1] Shin-ichiro Yanagiya,[1,2] Akihiro Shirai,[1,2] Masahito Niibe,[3] and Yoshitaka Nakano[4]

AFFILIATIONS

[1]Graduate School of Technology, Industrial and Social Sciences, Tokushima University, Tokushima 770-8506, Japan
[2]Institute of Post-LED Photonics, Tokushima University, Tokushima 770-8506, Japan
[3]Laboratory of Advanced Science and Technology for Industry, University of Hyogo, Kamigori, Hyogo 678-1205, Japan
[4]Department of Electrical and Electronic Engineering, Chubu University, Kasugai, Aichi 487-8501, Japan

[a]**Author to whom correspondence should be addressed:** retsuo@ee.tokushima-u.ac.jp

ABSTRACT

Enhanced photocatalytic activity of rutile-based TiO_2 materials under general lighting is practically desired. O_2 plasma-assisted annealing (PAA) effects on Pt-doped rutile TiO_2 nanoparticles were clarified along with its visible-light-driven photocatalytic activity enhancement. The PAA-treated samples were mainly analyzed using optical spectroscopy and x-ray photoelectron spectroscopy (XPS). The photocatalytic activity was assessed by decomposing methylene blue dye and inactivating *Bacillus subtilis* under general lighting. The PAA treatment changed the O 1s, Ti 2p, and Pt 4f spectra of XPS from those of the pristine sample. This change indicated that the PAA treatment introduced more oxygen deficiency or oxygen vacancies and more oxygen groups adsorbed on the surface. The introduced oxygen vacancies and adsorbed oxygen groups would change the band structure, which primarily narrowed the bandgap energy or broadened the valence band edge, increased the number of electron-trapping sites from the shallow to midgap levels, and enhanced the upward band-bending at the surface. The PAA-induced change in the band structure enhanced the decomposition and bacterial inactivation because it facilitated the separation and concentration of photoexcited carriers. The findings provide a new perspective on enhancing the photocatalytic activities of rutile-based TiO_2 nanoparticles under general lighting.

I. INTRODUCTION

Water and air pollution caused by organic contaminants and microbes is a growing global challenge that needs to be addressed as the world population increases.[1–10] This pollution harms ecosystems, raises health risks, and ultimately destabilizes society. To ensure water and air quality and achieve a sustainable society, water and air must be purified of organic contaminants and microbes. Therefore, efficient water and air purification technologies are essential for removing these pollutants from contaminated water and air.[11,12]

Semiconductors with photocatalytic activities have been attracting the most attention in removing organic contaminants and microbes from polluted water and air.[13–20] TiO_2-based semiconductors are some of the most promising photocatalysts because of their high photocatalytic activity, excellent stability, and nontoxicity.[21–26] Electrons and holes are generated when irradiated with photons at higher energies than the TiO_2 bandgap energy (3.0−3.2 eV) or with ultraviolet (UV) at wavelengths smaller than 400 nm.[27] Oxygen molecules (O_2) adsorbed on the TiO_2 surface can acquire the photogenerated electrons migrating to the surface. This migration leads to the generation of superoxide anions (O_2^-). Water molecules adsorbed on the TiO_2 surface can capture the photogenerated holes to form hydroxyl radicals (•OH). These reactive oxygen species (ROS) cause molecular chain breakage in organic compounds.[28] The generated ROS penetrate the bacteria cell envelope, oxidize membrane fatty acids, induce lipid peroxidation, oxidize proteins, and damage deoxyribonucleic acid.[29]

The high bandgap energy of TiO_2 (3.0−3.2 eV) hinders and restricts its use under visible light irradiation. Various photocatalytic technologies have been developed to solve this issue of limited visible light utilization. In particular, Pt doping of TiO_2 is an excellent technology to enhance the photocatalytic activity under visible light irradiation.[30–32] The Pt doping methods greatly narrow the bandgap energy and significantly increase the optical absorption in the visible light region, as compared with other metal doping.[26] The bandgap narrowing is thought to originate from the overlap of the valence band with the energy level newly formed by the d-orbital splitting.[32] For example, anatase TiO_2 doped with Pt greatly removes NO_x under visible light irradiation as compared with anatase/rutile-mixed TiO_2 (called P-25 supplied by Degussa Corp., Germany).[33] P-25 is an anatase-based TiO_2 composed of 80% anatase TiO_2 with a bandgap energy of 3.2 eV (a bandgap wavelength of 388 nm) and 20% rutile TiO_2 with a bandgap energy of 3.0 eV (a bandgap wavelength of 415 nm).[34]

However, rutile TiO_2 doped with Pt only inactivated bacteria such as *Escherichia coli* O157:H7 to the same extent as P-25 under visible light irradiation.[35] This is thought to originate from the shorter lifetime of photoexcited carriers in rutile TiO_2 (<1 ns) than that in anatase TiO_2 (>10 ns).[36,37] In other words, the recombination rate of photoexcited carriers is higher in rutile TiO_2. The shorter lifetime or higher recombination rate lowers the effective carrier concentration and, in turn, reduces the concentration of ROS generated. This reduction does not contribute to effectively enhance the photocatalytic activity. If the lifetime of photoexcited carriers in rutile TiO_2 was long, Pt doping would greatly inactivate the bacteria. Thus, a technology for extending the photoexcited carrier lifetime in rutile TiO_2 is required to enhance the photocatalytic activity of rutile TiO_2 doped with Pt.

In previous studies, we clarified the O_2 plasma-assisted annealing (PAA) effect on the photocatalytic activity of anatase-based TiO_2.[38,39] The PAA enhanced the decomposition of methylene blue (MB) dye and inactivation of *Bacillus subtilis* (*B. subtilis*) on anatase TiO_2 under UV irradiation.[38] The PAA also enhanced the dye decomposition and bacterial inactivation of P-25 under UV irradiation and visible light irradiation at a wavelength of 405 nm, unlike the thermal annealing that did not enhance those of P-25 under UV irradiation.[39] The dominant factor for the PAA-induced enhancement is the introduction of oxygen vacancies, which trap the photogenerated electrons.[38,39] The trapping lowers the carrier recombination rate, thus prolonging the carrier lifetime.[40] However, we did not demonstrate whether the PAA treatment enhances the photocatalytic activity of rutile TiO_2 under visible light irradiation. Therefore, a more detailed understanding of the interactions between the PAA treatment and rutile TiO_2 is required to enhance the visible-driven photocatalytic activity of rutile-based TiO_2.

The present study investigates the effect of O_2 PAA treatment on Pt-doped rutile TiO_2 and its enhanced photocatalytic activity under visible light irradiation. The Pt-doped rutile TiO_2 used consisted of 0.1 wt. % Pt-doped rutile TiO_2 nanoparticles (MPT-623) supplied by Ishihara Sangyo Co., Japan.[41] The PAA treatment was performed using a dielectric barrier discharge plasma device equipped with a heater, developed by Kawakami *et al.*[42] For compassion, thermal annealing was also investigated using an electric furnace. The visible light sources used were white light-emitting devices (white LEDs), commonly used as general lighting sources. The photocatalytic activities of treated samples were evaluated by measuring the decomposition of MB dye and inactivation of *B. subtilis* under white LED irradiation. The concentrations of photoexcited carriers were qualitatively analyzed by subtracting the electrical conductivities of nonirradiated samples from those irradiated with white LED light. The crystallization features of treated samples were measured using x-ray diffraction (XRD). The surface morphologies of treated surfaces were observed using scanning electron microscopy (SEM). The chemical compositions of treated surfaces were examined by x-ray photoelectron spectroscopy (XPS). These physical and chemical characteristics enable discussion of the photocatalytic activity enhancement. The present study is of great importance for a comprehensive understanding of the enhanced photocatalytic activities of Pt-doped rutile TiO_2 nanoparticles under white LED irradiation. Our findings also provide information for the industrial fabrication of Pt-doped rutile TiO_2 nanoparticles with high decomposition efficiency and antibacterial activity under general illumination.

II. EXPERIMENTAL SETUP AND METHODOLOGY

A. Photocatalytic materials

The photocatalytic samples used were 0.1% Pt-doped rutile TiO_2 nanoparticles called MPT-623,[41] as described in Sec. I. The MPT-623 nanoparticles were immobilized on a glass substrate to improve sample handling. The surface of the glass substrate with an area of $12.5 \times 12.5\ mm^2$ was treated with a capacitively-coupled argon plasma at 60 Pa for 10 min to enhance the wettability of the glass surface. After irradiation, 100 μl of MPT-623 dispersion solution with a concentration of 2.5×10^3 mass ppm was dropped onto the plasma-irradiated glass surface and allowed to dry naturally for at least one day. The thickness of MPT-623 immobilized on the glass was estimated to be approximately 380 nm using a mass density of rutile TiO_2 of $4.2\ g/cm^3$.[42,43] The method of immobilizing MPT-623 was the same as that used in immobilizing P-25.[39]

B. PAA treatment

A dielectric barrier discharge plasma reactor with a heater[42] was used to perform the PAA treatment of MPT-623 nanoparticles. The reactor has two stainless electrodes: the electrically powered and grounded electrodes. The discharge gap length between these two electrodes was 2 mm. O_2 gas with a purity of 99.9 vol. % was fed into the reactor with a flow rate of 15 ml/min. The pressure inside the reactor was maintained at 100 kPa by a rotary pump. The MPT-623 immobilized on the glass substrate was placed on the grounded electrode with a diameter of 40 mm. This electrode was heated from room temperature to 300 °C and kept at 300 °C using a heater. Then, the other electrode covered with an alumina dielectric with a diameter of 50 mm was powered with a 25 kHz sinusoidal wave with a maximum voltage of 1.5 kV to generate a low-temperature O_2 plasma. The maximum value of electric current flowing into the sample was 100 mA. The electric power consumption was approximately 8 W by multiplying the voltage and current waveforms and then integrating them over one period.

The treatment time of PAA was 1 h. Further details of PAA treatment can be found in our literature.[38,42]

For comparison, MPT-623 nanoparticles were irradiated only with a low-temperature O_2 plasma without external heating, using the same plasma reactor used for the PAA treatment. The conditions for the plasma generation were the same as those for the PAA treatment except for external heating. The samples were also annealed for 1 h at 300 °C in O_2 gas at 100 kPa without generating O_2 plasma in the same plasma reactor. Furthermore, the samples were annealed for 1 h at temperatures from 300 to 500 °C in ambient air with an electric furnace.

C. Photocatalytic activities

The decomposition of MB dye and inactivation of *B. subtilis* under visible light irradiation were assessed for the photocatalytic activities of MPT-623 nanoparticles. The light sources used were white LEDs, i.e., general lighting sources, that emitted an optical spectrum consisting mainly of two peaks at 450–470 nm and 550–560 nm.[44] The spectrum of the white LED used will be shown in Fig. 3(a) in Sec. III. For the MB dye decomposition, the light intensity emitted from the LEDs was set to 6×10^3 lx at the sample surface. The volume and concentration of MB dye solution used were 4 ml and 10 mass ppm, respectively. Before light irradiation, the samples were immersed in the MB dye solution for 1 h in the dark until adsorption equilibrium was reached. The immersed samples were then irradiated with white LEDs for 8 and 16 h. The reduction in the MB dye concentration was assessed by measuring the decrease in the absorbance peak intensity at a wavelength of 664 nm using a spectrophotometer (Photal MCPD-370A, Otsuka Electronics, Japan). This reduction was estimated as the MB dye decomposition value, $\ln(C/C_0)$, where C was the MB dye concentration at a given irradiation time and C_0 was the MB dye concentration before light irradiation.

For the assessment of the bacterial inactivation, the white LED light intensity was set to 1×10^4 lx at the sample surface. The bacterium used was *B. subtilis* American Type Culture Collection 6633.[45] An aliquot of the bacterial suspension (0.01 ml) with 2×10^6 colony-forming units per ml (CFU/ml) was dropped onto the sample surface. Then, the sample surface was irradiated with white LEDs for 0 and 2 min. After light irradiation, the samples were immersed for 1 min in 10 ml of soybean-casein digest lecithin polysorbate (SCDLP) broth to extract the bacteria from the sample surfaces into the SCDLP broth. The SCDLP broth (0.1 ml) containing the bacteria was diluted serially 10-fold with the SCDLP broth. The diluted broths were dropped on agar plates of SCDLP and incubated for 24 h at 37 °C. After incubation, the common log numbers of viable cells grown on the agar were determined using the colony counting method.[39,46] The bacterial inactivation was performed in triplicate for each sample, and then the data were averaged.

D. Characterization of PAA-treated photocatalytic materials

The optical absorbance values of the samples, a, were measured using UV-visible light absorption spectroscopy (U-3900, Hitachi, Japan). The bandgap energies of the samples were evaluated based on the Tauc method using the measured absorbance values.[47–49] The electrical conductivities of the samples under white LED irradiation and nonirradiation were assessed to estimate the concentration of photoexcited carriers qualitatively using electrical impedance spectroscopy (3522 lCR HiTESTER, Hioki, Japan). The photoluminescence (PL) of the samples was measured at various temperatures with an excitation light of 313 nm in wavelength (4 eV in photon energy) using a spectrometer employing a charge-coupled device detector (i-trometer, BWTEK). The sample temperature was controlled using a cryostat system.

The surface morphologies of the samples were observed with SEM (JSM-6510A, JEOL). The root mean square (RMS) values of sample surface roughness were analyzed in a scanning area of $10 \times 10\,\mu m^2$ using an atomic force microscope (AFM, AFM5500M, Hitachi High-Technologies, Japan). The XRD patterns were measured with Cu Kα radiation at an energy of 8048 eV using XRD (RINT-2200/PC, Rigaku, Japan) to assess the crystallinity of the samples. Ti 2p, O 1s, and Pt 4f peaks from the surfaces were measured with Al Kα radiation of an energy of 1486.6 eV using XPS (PHI500, Ulvac-Phi, Japan) to assess the chemical compositions of the samples.

III. RESULTS

Figure 1(a) shows the white LED-induced MB dye decomposition values, $\ln(C/C_0)$, of the pristine, PAA-treated, O_2-plasma-only-treated, and O_2-gas-annealed samples. A large MB dye decomposition signifies a small value of $\ln(C/C_0)$. The decrease in $\ln(C/C_0)$ in the gray area shows a reduction of MB dye concentration due to adsorption because the data in that area were measured without white LED irradiation. The $\ln(C/C_0)$ value of the pristine sample hardly changes even when the adsorption time extends from 0 to 1 h. However, the PAA-treated sample has the smallest value of $\ln(C/C_0)$ at an adsorption time of 1 h among the treated samples. The comparison between the results indicates that the PAA treatment greatly enhances the MB dye adsorption of rutile-based TiO_2 nanoparticles as compared with the other treatments. Even under the white LED irradiation, the PAA-treated sample also has the smallest value of $\ln(C/C_0)$ as the irradiation time extends. For example, at an irradiation time of 16 h, the $\ln(C/C_0)$ value of the PAA-treated sample is approximately two times smaller than that of the pristine sample. The $\ln(C/C_0)$ values of the O_2-plasma-only-treated and O_2-gas-annealed samples are almost identical and are approximately 1.5 times smaller than that of the pristine sample. Specifically, the PAA-treated sample exhibits the largest MB dye decomposition rate, defined by the decrease in $\ln(C/C_0)$ per hour, $-4.3 \times 10^{-2}\,h^{-1}$; the decomposition rates of the O_2-plasma-only-treated, O_2-gas-annealed, and pristine samples are -3.5×10^{-2}, -3.6×10^{-2}, and $-2.8 \times 10^{-2}\,h^{-1}$, respectively. The comparison indicates that the PAA treatment significantly enhances the MB dye decomposition of rutile-based TiO_2 nanoparticles compared to the other treatments.

Figure 1(b) shows the white LED-induced MB dye decomposition values, $\ln(C/C_0)$, of the samples annealed in ambient air at various temperatures. The $\ln(C/C_0)$ value decreases as the temperature increases to 300 °C but increases with further increasing temperature. In particular, the $\ln(C/C_0)$ value of the sample annealed at 500 °C is similar to that of the pristine sample. The result

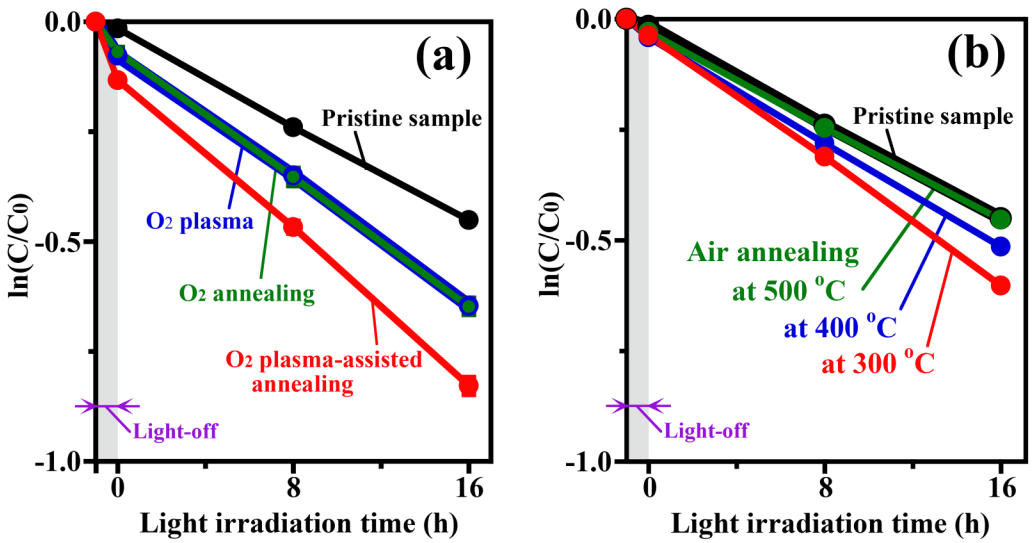

FIG. 1. MB dye decomposition values, $\ln(C/C_0)$, of (a) the pristine, PAA-treated, O_2-plasma-only-treated, O_2-gas-annealed samples, and (b) air-annealed samples under white LED irradiation. The data in the gray areas in the figures represent the results in the absence of white LED irradiation.

indicates that the sample annealed at 300 °C has the largest MB dye decomposition rate, $-3.5 \times 10^{-2}\,h^{-1}$. However, this rate is similar to those of the O_2-plasma-only-treated and O_2-gas-annealed samples and is smaller than that of the PAA-treated sample. Thus, the PAA treatment is found to be more effective in enhancing the white LED-induced decomposition of rutile-based TiO_2 nanoparticles, as in the case of anatase-based TiO_2 nanoparticles (P-25).[38,39]

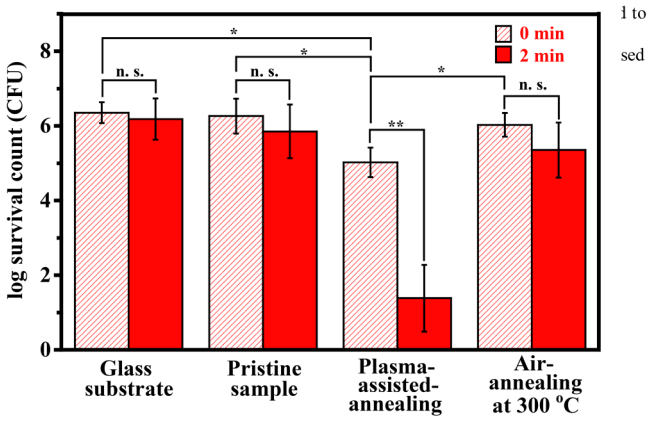

FIG. 2. Log numbers of bacterial survival for the glass substrate, the pristine, PAA-treated, and 300 °C-air-annealed samples under white LED irradiation for 0 and 2 min. Data are presented as means ± standard deviation (the number of times = 3). The abbreviation, n. s., signifies no significant differences, as estimated by the two-tailed and unpaired Student's *t*-test. The symbols ** and * correspond to a *P*-value < 0.01 and a *P*-value < 0.05, respectively, as estimated by the *t*-test.

Figure 2 shows the log numbers of bacterial survival of the glass substrate, pristine, PAA-treated, and 300 °C-air-annealed samples. A high bactericidal efficacy signifies a low log number of bacterial survival. The data for 0 min represent the survival numbers without white LED irradiation. In the absence of light irradiation, the samples except for the PAA-treated sample have similar survival numbers. The survival number of the PAA-treated sample is lower than those of the other samples. The comparison suggests that the PAA-treated sample inactivates *B. subtilis* by one order of magnitude, even without light irradiation. This inactivation would be connected to more oxygen groups adsorbed on the surface, as shown later by the XPS data. When irradiated with white LED irradiation for 2 min, the survival number of the PAA-treated sample is much lower than that of the glass substrate, but the survival numbers of the other samples are similar. Specifically, the PAA-treated sample inactivates *B. subtilis* by 4–5 orders of magnitude under white LED irradiation or 2 min, whereas the other samples hardly inactivate *B. subtilis*. The result indicates that the PAA treatment greatly enhances the bacterial inactivation of rutile-based TiO_2 nanoparticles as compared to the other treatment.

Figure 3(a) shows the absorbance values of the pristine, PAA-treated, and 300 °C-air-annealed samples. The spectrum of the white LED used is also shown in the figure. The absorbance value of the PAA-treated sample is larger than those of the pristine and annealed samples. In particular, this trend is more pronounced in the visible light range. For example, at wavelengths of 450–470 nm, the absorbance value of the PAA-treated sample is 1.3 times larger. The result indicates that the PAA treatment greatly enhances the visible-light absorption of rutile-based TiO_2 nanoparticles as compared with the air-annealing treatment. Figure 3(b) compares the Tauc plots of $(ahv)^2$ for the treated samples, where h is the Planck constant and v is the photon frequency. The optical bandgap energies of rutile-based

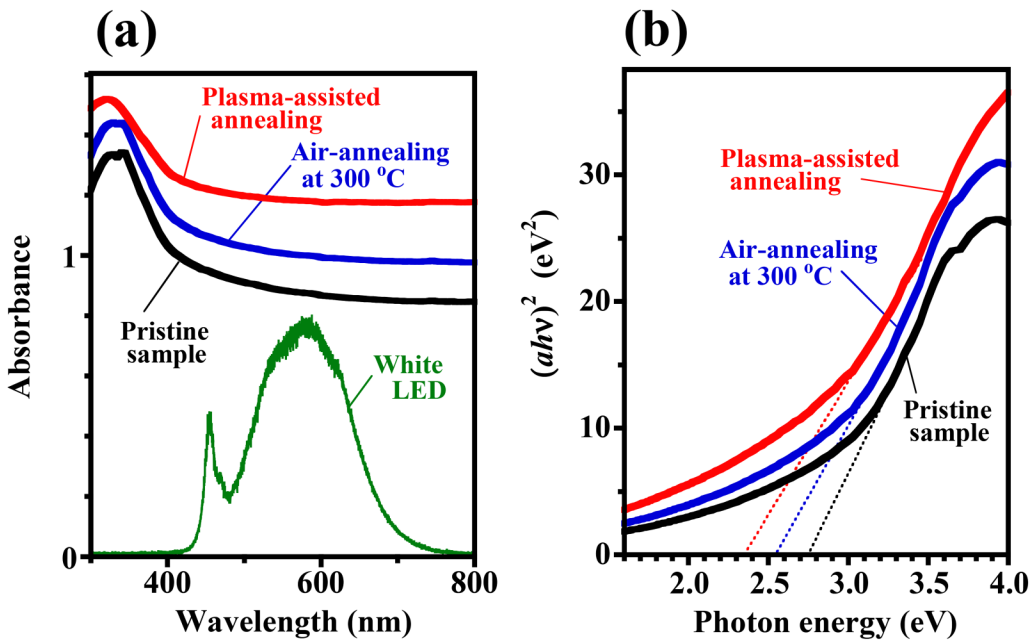

FIG. 3. (a) Absorbance values of the pristine, PAA-treated, and 300 °C-air-annealed samples. The bottom curve corresponds to the spectrum of white LED used. (b) Tauc plots of $(ahv)^2$ as a function of photon energy for the pristine, PAA-treated, and 300 °C-air-annealed samples.

TiO_2 nanoparticles with the direct transition bandgaps are extrapolated using the Tauc plots.[50,51] The bandgap energy of the pristine sample is estimated to be approximately 2.75 eV (451 nm in wavelength). This value is narrowed from the bandgap energy of rutile TiO_2, 3.0 eV, by Pt doping, as is consistent with the literature.[51,52] In other words, the optical absorption edge of rutile TiO_2 is red-shifted from 415 to 451 nm by Pt doping. The two post-treatments further narrow the bandgap energy. In particular, the narrowing trend is remarkable for the PAA-treated sample. The bandgap energy of the PAA-treated sample, 2.35 eV (528 nm in wavelength), is smaller than that of the air-annealed sample, 2.55 eV (486 nm). This result suggests that the PAA-treated sample absorbs visible light with longer wavelengths more strongly than the other samples. Specifically, the light with wavelengths between 400 and 528 nm emitted from the white LEDs is strongly absorbed by the PAA-treated sample. The narrowing of the bandgap energy would be attributed to the introduction of more oxygen vacancies in TiO_2 due to the PAA treatment, which will be described along with the XPS and PL data later. The oxygen vacancies create unpaired electrons associated with Ti^{3+} species, introducing donor levels within the bandgap.[53–55] The occurrence of a continuum of oxygen vacancy states within the bandgap contributes to the broadening of the valence band edge, thus narrowing the bandgap energy.[53–55] Thus, the PAA treatment is found to greatly narrow the bandgap energy of rutile-based TiO_2 nanoparticles as compared with annealing treatment.

Figure 4 shows the electrical conductivities in the presence and absence of the white LED irradiation for the pristine,

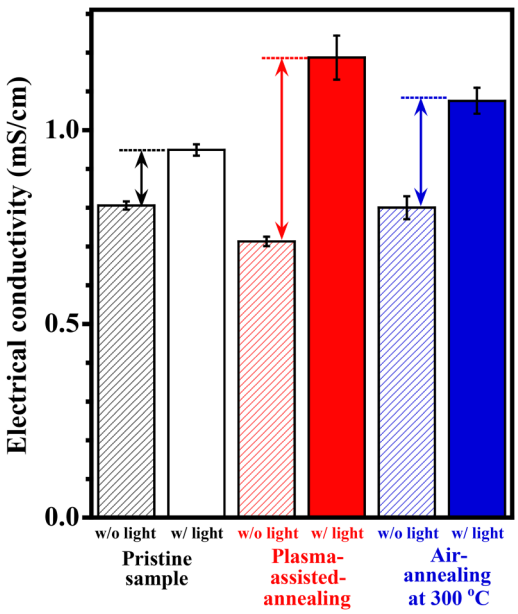

FIG. 4. Electrical conductivities of the pristine, PAA-treated, and 300 °C-air-annealed samples with and without white LED irradiation. The arrows in the figure correspond to the photon-induced electrical conductivities of the samples.

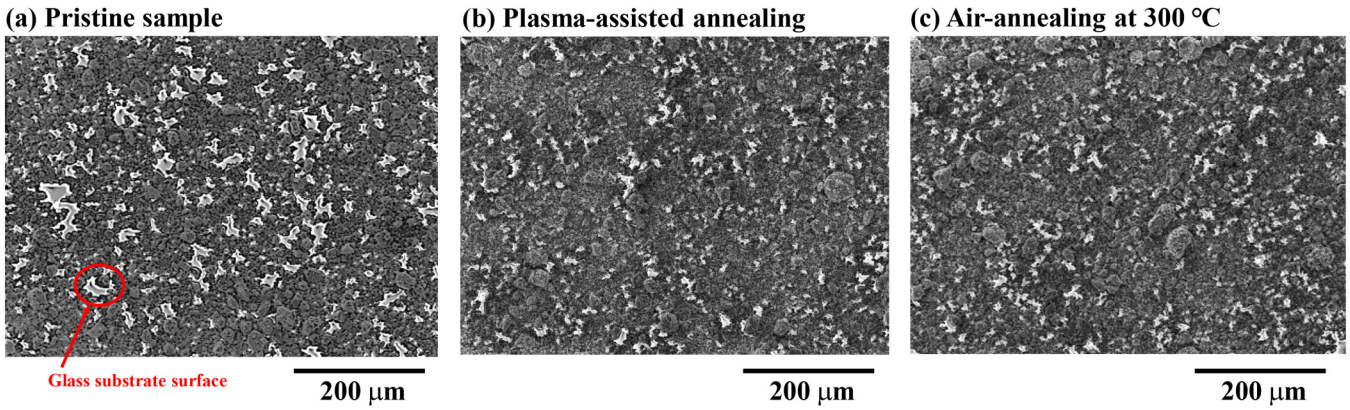

FIG. 5. SEM images of the surfaces of (a) the pristine, (b) PAA-treated, and (c) 300 °C-air-annealed samples. The whitish-gray or white color portion in the circle corresponds to the surface of glass substrate without the rutile-based TiO_2 nanoparticles. This portion can be found everywhere on the surface of each sample.

PAA-treated, and 300 °C-air-annealed samples. The difference between these two conductivities for each sample represents the photon-induced conductivity proportional to the concentration of photoexcited carriers. The photon-induced conductivity of the PAA-treated sample is higher than those of the pristine and 300 °C-air-annealed samples. This result indicates that more photoexcited carriers are produced in the PAA-treated sample irradiated with white LEDs. Thus, the PAA treatment enhances the photoexcited carrier concentration of rutile-based TiO_2 nanoparticles under white LED irradiation.

Figure 5 shows the SEM images of the surfaces of the pristine, PAA-treated, and 300 °C-air-annealed samples. There are lots of whitish-gray or white portions on the surface of the pristine sample. These portions are the surface of the glass substrate on which the rutile-based TiO_2 nanoparticles are not present. The other portions are the rutile-based TiO_2 nanoparticles agglomerated on the glass surface. The aggregates of various sizes appear to be somewhat locally distributed on the glass surface. This distribution differs from that of anatase-based TiO_2 nanoparticles (P-25) uniformly distributed on the glass surface.[38,39] The SEM images of the PAA-treated and air-annealed samples resemble each other but differ from that of the pristine sample. The PAA and air-annealing treatments greatly reduce the area of one whitish-gray or white portion and increase the number of those portions as compared with the pristine sample. The change in the surface morphology due to the post-treatments may originate from the thermal diffusion of rutile phase particles because of their relatively larger thermal conductivity.[56] In response to the change in the surface morphology, the RMS surface roughness is also changed. The PAA treatment and 300 °C air-annealing increase the RMS surface roughness from 794 to 910 and 819 nm, respectively. Notably, the surface roughness of the PAA-treated sample is larger. The increased surface roughness generally facilitates optical scattering, thereby enhancing optical absorption. Thus, the PAA-induced change in the morphology would contribute to the increased optical absorption [Fig. 3(a)].

Figure 6 shows the XRD patterns of the pristine, PAA-treated, and 300 °C-air-annealed samples. These data were superimposed on a halo pattern of the glass substrate. The XRD pattern of the pristine sample consists of (110), (101), (111), (220), and (211) plane orientations of the rutile phase crystalline structure with lattice parameters, $a = b = 4.59$ Å and $c = 2.96$ Å.[57,58] The average size of the pristine rutile nanoparticles was calculated to be 16 nm

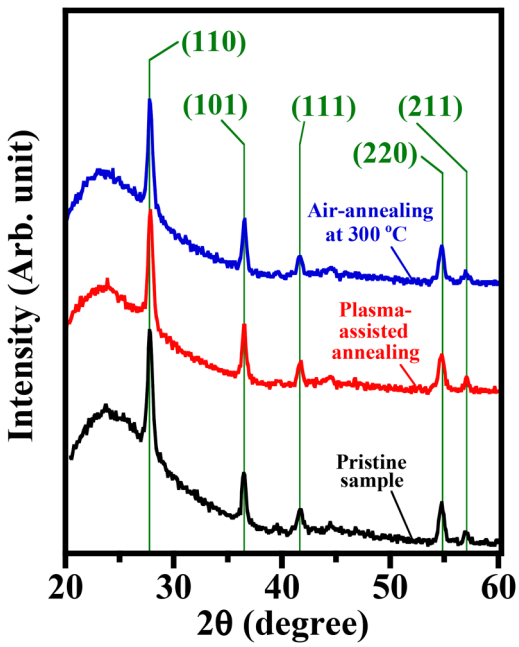

FIG. 6. XRD patterns of the pristine, PAA-treated, and 300 °C air-annealed samples.

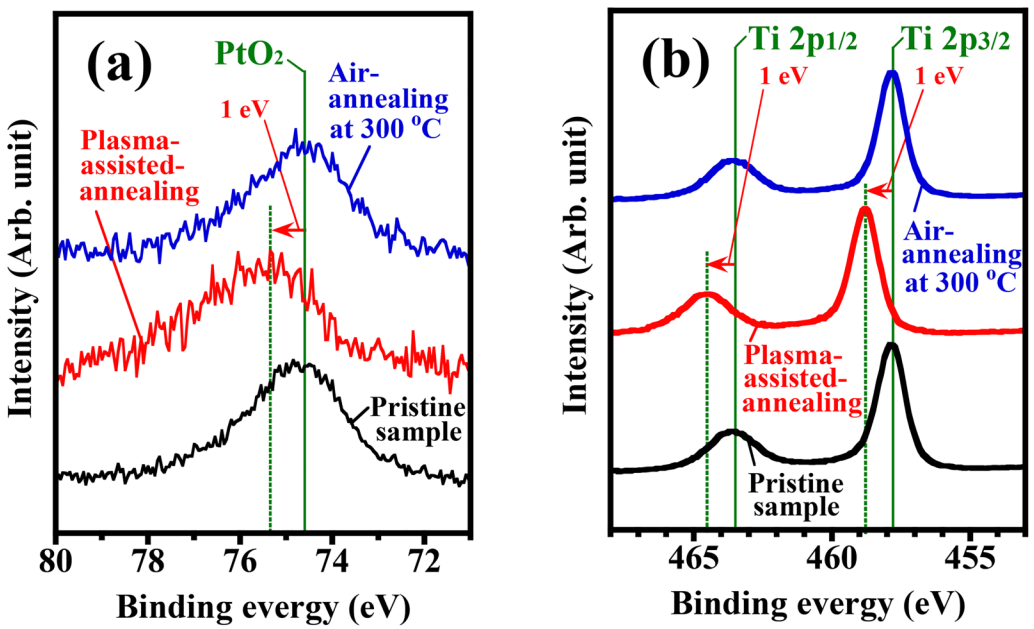

FIG. 7. (a) Pt 4f and (b) Ti 2p regions in XPS spectra of the pristine, PAA-treated, and 300 °C-air-annealed samples.

using the Scherrer formula, $0.9\lambda/(\beta\cos\theta)$. Here, λ is the wavelength of the x ray, 1.5406 Å, β is the half-width of the (110) plane orientation peak intensity, $0.56 \times \pi/180$ rad, and θ is the diffraction angle of the (110) plane orientation, 27.46°.[59,60] The estimated particle size is roughly similar to that of the anatase-based TiO_2 nanoparticles, P-25 (20 nm).[61] The XRD patterns of the PAA-treated and air-annealed samples consist of the same plane orientations as that of the pristine sample. This result suggests that the PAA treatment does not change the rutile phase crystalline structure and the nanoparticle size, as in the case of air-annealing.

Figure 7 shows the Pt 4f and Ti 2p regions of the measured XPS spectra of the pristine, PAA-treated, and 300 °C-air-annealed samples. The Pt 4f spectrum of the pristine sample consists of a peak at a binding energy of 74.6 eV, which is associated with the formation of PtO_2.[62] The Ti 2p spectrum of the pristine sample consists of two peaks at binding energies of 457.8 and 463.5 eV, which are associated with Ti $2p_{3/2}$ and Ti $2p_{1/2}$ due to the Ti–O bond in the TiO_2 lattice, respectively.[63,64] The Pt 4f and Ti 2p spectra of the air-annealed sample are the same as those of the pristine sample. However, the spectra of the PAA-treated sample shift to higher energy sides by 1 eV. This change suggests that an increase in oxygen vacancies increases the amount of oxygen groups adsorbed on the surface, resulting in higher oxidation states of Pt–O and Ti–O.[65,66] Thus, the PAA treatment influences the chemical states of Pt 4f and Ti 2p, whereas the air-annealing does not.

There is a different trend for the chemical states of O 1s. Figure 8 shows the O 1s regions of measured XPS spectra of the samples (open circles). The O 1s spectrum of the pristine sample consists of two peaks at binding energies of approximately 530 and 532 eV, which are associated with the O–Ti bond in the TiO_2 lattice and the terminal oxygen groups adsorbed on the surface, respectively.[67,68] The peak intensity of the O–Ti bond is larger than that of the adsorbed oxygen groups. The O 1s spectrum of the PAA-treated sample also consists of the same peaks but shifts to a higher energy side by 1 eV. Moreover, the peak intensity associated with the adsorbed oxygen groups is larger. This result suggests that more oxygen groups are adsorbed onto the surface by an increase in oxygen vacancies caused with O_2 plasma irradiation.[65,66] In contrast, the O 1s spectrum of the air-annealed sample resembles that of the pristine sample, suggesting that air-annealing does not contribute to increasing the amount of adsorbed oxygen groups.

To gain a deeper understanding of the chemical states, we decomposed the measured O 1s spectra of Fig. 8 into three pseudo-Voigt functions located at binding energies of 529.7 eV due to the O–Ti bond (blue curves in Fig. 8), 531.0 eV due to the bridging oxygen groups (green curves), and 532.3 eV due to the adsorbed oxygen groups (purple curves), respectively.[67,68] This peak decomposition was performed such that the sum of the pseudo-Voigt functions (black curves) was fitted to the measured O 1s spectra, as shown in Fig. 8. Figure 9 shows the O/Ti ratios of the O–Ti bond, bridging oxygen groups, and terminal oxygen groups, which are determined by multiplying the total O/Ti ratio by their fractions estimated from the peak decomposition, respectively. The total O/Ti ratio is defined as the ratio of the integrated intensity of the measured O 1s spectrum to that of the measured Ti 2p spectrum. For the pristine sample, the O/Ti ratio of the O–Ti bond is approximately 2, almost fulfilling the stoichiometry condition. The O/Ti ratio of terminal oxygen groups is smaller than that of the O–Ti bond but larger than that of the bridging oxygen groups. This result suggests that the surface of the pristine sample is dominated by the

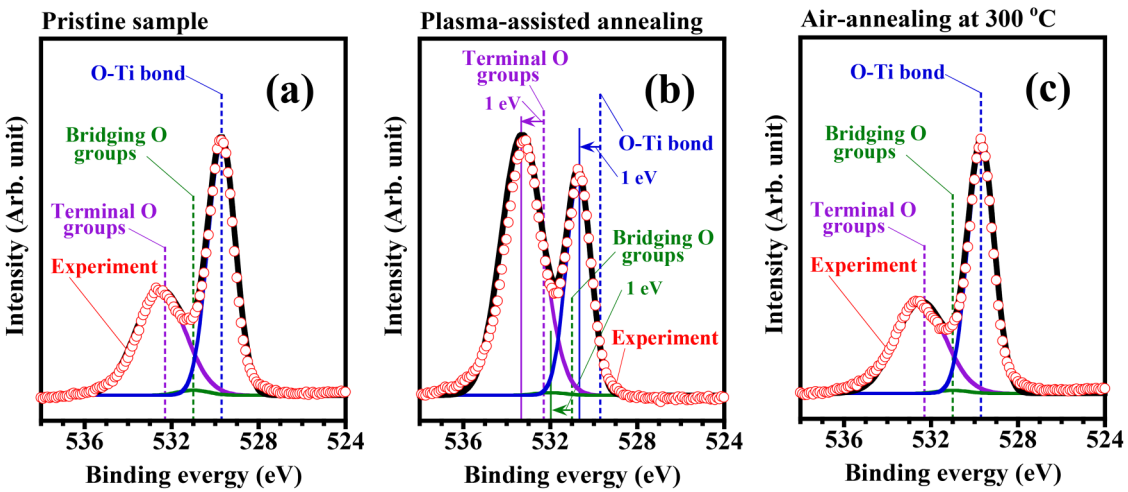

FIG. 8. O 1s regions in XPS spectra of (a) the pristine, (b) PAA-treated, and (c) 300 °C-air-annealed samples.

adsorbed terminal oxygen groups, with no bridging oxygen groups present. The two post-treatments decrease the O/Ti ratio of the O−Ti bond. In particular, this decreasing trend is more significant in the PAA treatment: the PAA treatment reduces the number of lattice oxygen atoms by approximately 12%. This result indicates that more lattice oxygen deficiency or oxygen vacancies are introduced in the rutile-based TiO_2 nanoparticles with the PAA treatment. In the case of the bridging oxygen groups, there are no post-treatment effects; the O/Ti ratio hardly changes from that of the pristine sample. The PAA treatment increases the O/Ti ratio of the terminal oxygen groups from 1.5 to 3.5, but the air-annealing hardly changes the O/Ti ratio. This result suggests that the terminal oxygen groups, such as O_2 and O from the O_2 plasma,[38] are supplied to the surface with the PAA treatment. Specifically, the PAA treatment increases the adsorbed oxygen groups by approximately twofold. The increase in the terminal oxygen groups is consistent with the literature: oxygen groups are readily adsorbed on the oxygen vacancy sites to capture or share electrons located on the sites.[69–72] Thus, the PAA treatment is found to introduce more lattice oxygen efficiency or oxygen vacancies as well as more adsorbed terminal oxygen groups into rutile-based TiO_2 nanoparticles.

Figure 10 shows the temperature dependences of PL spectra from the pristine, PAA-treated, and 300 °C-air-annealed samples. In the case of the pristine sample at 15 K, there are two emission

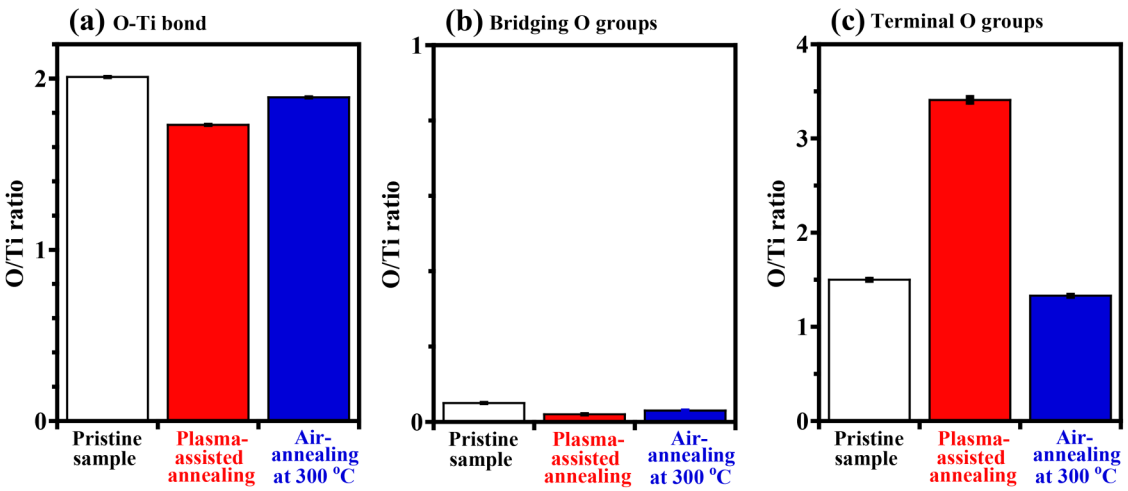

FIG. 9. O/Ti ratios of (a) O−Ti bond, (b) bridging oxygen groups, and (c) terminal oxygen groups for the pristine, PAA-treated, and 300 °C-air-annealed samples.

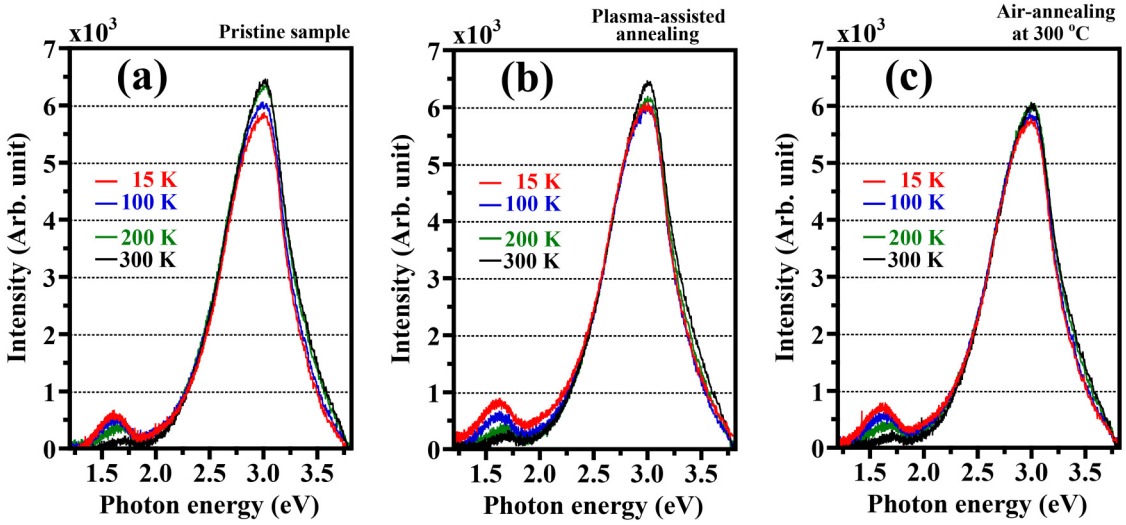

FIG. 10. Temperature dependence of PL spectra from (a) the pristine, (b) PAA-treated, and (c) 300 °C-air-annealed samples.

peaks at photon energies of 1.6 and 3 eV in the PL spectrum. The emission peak at 3 eV originates from the radiative recombination of free excitons in rutile TiO_2.[73] The peak intensity slightly increases as the temperature rises from 15 to 300 K. This is termed negative thermal quenching, which would be attributed to part of the thermal energy being changed into light radiative energy by phonons.[74] The emission peak at 1.6 eV in the PL spectrum originates from the radiative recombination between midgap trapped electrons and free holes in rutile TiO_2.[75] The midgap trapping of electrons would be attributed to oxygen vacancies located at 0.75 −1.18 eV below the conduction band edge of TiO_2.[71,75,76] The peak intensity decreases with shifting to the higher-photon energy side as the temperature rises from 15 to 300 K. This is termed thermal quenching, which results from the nonradiative relaxation of excited electrons to the ground state.[77] The temperature dependences of the two peak intensities of PAA-treated and air-annealed samples are similar to those of the pristine sample. However, when compared in detail, their peak intensity values at each temperature differ from those of the pristine sample. In particular, at a low temperature of 15 K, the 1.6 eV peak intensity of the PAA-treated sample is the largest among them. This comparison suggests that the PAA treatment introduces more oxygen vacancies at the midgap level in the rutile-based TiO_2 nanoparticles.

IV. DISCUSSION

The PAA treatment of Pt-doped rutile-based nanoparticles greatly enhances the dye decomposition and bacterial inactivation under white LED irradiation, as compared with the other post-treatments (Figs. 1 and 2). This enhancement would be attributed predominantly to the increased photocatalytic activity of Pt-doped rutile TiO_2 particles because the photon-induced conductivity associated with the photoexcited carrier concentration is the largest for the PAA-treated sample (Fig. 4), as in the case of anatase-based TiO_2 nanoparticles (P-25).[39] This fact suggests that the PAA treatment is highly effective in enhancing the photocatalytic activities regardless of the TiO_2 crystallinity, i.e., the rutile and anatase phases.

The largest concentration of photoexcited carriers would be due to the change in the band structure of Pt-doped rutile-based nanoparticles, originating from the PAA-induced change in the O 1s, Ti 2p, and Pt 4f spectra of XPS (Figs. 7–9). The changed XPS spectra indicate that the PAA treatment introduces more oxygen vacancies and more terminal oxygen groups adsorbed on the surface. The increased amount of the oxygen vacancies is also supported by the increased PL peak intensity of around 1.6 eV at a low temperature of 15 K (Fig. 10). This amount of oxygen vacancies is estimated to be approximately four times larger than that in anatase-based TiO_2 nanoparticles (P-25) because the PAA treatment reduces the number of lattice oxygen atoms in P-25 by 3%.[39] The amount of oxygen groups adsorbed on the rutile-based TiO_2 nanoparticles is also estimated to be approximately twice as large as that in P-25.[39] The comparison suggests that the PAA-treated rutile-based TiO_2 nanoparticles have more oxygen vacancies and more adsorbed oxygen groups than the PAA-treated anatase-based TiO_2 nanoparticles do. The oxygen-related behavior significantly changes the band structure of rutile-based TiO_2 nanoparticles.

The PAA-introduced amount of more oxygen vacancies contributes to narrowing the bandgap energy or broadening the valence band edge of Pt-doped rutile TiO_2 nanoparticles (Fig. 3) and increasing the number of electron-trapping sites from the shallow to midgap levels (Fig. 10), as described in Sec. III. The PAA-introduced amount of more oxygen groups adsorbed with capturing electrons[69–72] contributes to facilitating the upper band-bending.[71,78] This electron capturing is supported by the lower electrical conductivity of the PAA-treated sample in the absence of

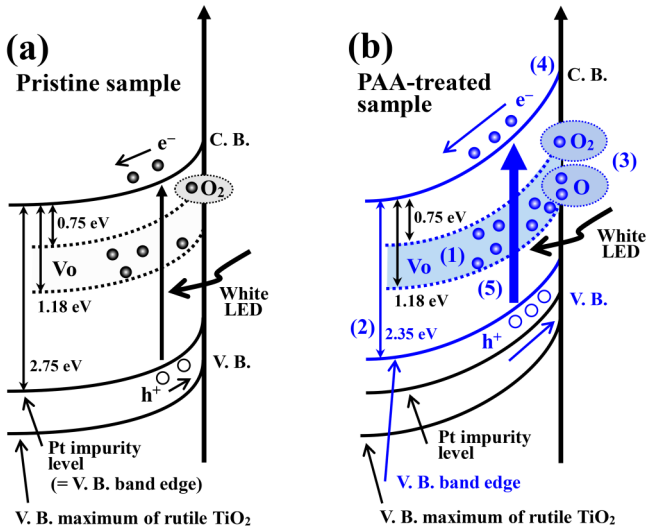

FIG. 11. Proposed energy band structure model of (a) Pt-doped rutile TiO_2 nanoparticles and (b) Pt-doped rutile TiO_2 nanoparticles treated by PAA. The blue portions in (b) correspond to the changes induced by the PAA treatment. The abbreviations, C.B. and V.B. signify the conduction and valence bands, respectively. The PAA treatment introduces a continuum of more oxygen vacancies (1) trapping electrons within the bandgap, which narrows the bandgap energy or broadens the valence band edge (2) and increases the amount of adsorbed oxygen groups such as O_2 and O (3). The bandgap narrowing (2) contributes to an increase in the optical absorption (4), which increases the concentration of photoexcited carriers. The increased amount of adsorbed oxygen groups (3) facilitates the upper band bending at the surface (5), leading to enhanced charge separation.

white LED irradiation (Fig. 4). Thus, the PAA treatment is considered to significantly change the band structure of Pt-doped rutile TiO_2 nanoparticles to enhance the concentration of photoexcited carriers, as shown in Fig. 11. When irradiated with white LEDs, the amount of optical absorption is increased by the bandgap narrowing or the valence band edge broadening. This increase leads to increasing the concentration of photoexcited carriers. The photogenerated electrons are trapped by more oxygen vacancies introduced at the shallow to midgap levels. The photogenerated holes migrate to the surface due to the increased upper band bending. These carrier behaviors lead to the charge separation, suppressing the recombination. As a result, the concentration of photoexcited carriers increases, causing more ROS that decompose chain breakage in organic compounds or that penetrate the bacterial cell envelope with damage. This contributes to the PAA-enhanced photocatalytic activities, i.e., the enhanced dye decomposition and bacterial inactivation.

The PAA treatment has another effect on the surface of rutile-based TiO_2 nanoparticles. The PAA treatment increases the MB dye adsorption (Fig. 1). The increased MB dye adsorption would be related to more oxygen groups adsorbed on the surface (Figs. 7–9). The adsorbed oxygen groups constitute functional polar groups with high wettability and adhesive properties.[79–81] Thus, more adsorbed oxygen groups induced by the PAA treatment would also affect the increased MB dye adsorption. This result suggests that the PAA treatment has a high possibility of enhancing the wettability of polymers such as polypropylene.[79–81] Furthermore, the adsorbed oxygen groups would also be associated with the PAA-induced bacterial inactivation without light irradiation (Fig. 2). The adsorbed oxygen groups may contain a small amount of ROS, such as H_2O_2 having a long lifetime.[82] The presence of this small amount would contribute to bacterial inactivation under nonirradiation.

V. SUMMARY AND CONCLUSIONS

We have clarified the PAA treatment effect on Pt-doped rutile TiO_2 nanoparticles and its photocatalytic activity under white LED irradiation used as general lighting. The PAA treatment significantly changes the O 1s spectrum of XPS from that of the pristine sample and shifts the O 1s, Ti 2p, and Pt 4f XPS spectra to the higher energy sides. This change indicates that the PAA treatment introduces more oxygen vacancies and more terminal oxygen groups adsorbed on the surface. The change in the XPS spectra would contribute to a change in the band structure of rutile-based TiO_2 nanoparticles to enhance the separation and concentration of photoexcited carriers. The PAA-introduced amount of more oxygen vacancies contributes not only to narrowing the bandgap energy or broadening the valence band edge but also to increasing the density of electron-trapping sites from the shallow to midgap levels. The PAA-introduced amount of more oxygen groups adsorbed with capturing electrons contributes to facilitating the formation of the upper band-bending. The PAA-induced change in the band structure greatly enhances the photocatalytic activities of the dye decomposition and bacterial inactivation because it facilitates the separation and concentration of photoexcited carriers, as compared with air-annealing, O_2-annealing, and O_2 plasma-only treatment. Our finding provides a new perspective on enhancing the photocatalytic activities of rutile-based TiO_2 nanoparticles

ACKNOWLEDGMENT

Part of this work was supported by JSPS KAKENHI Grant No. 20K03917.

AUTHOR DECLARATIONS

Conflict of Interest

The authors have no conflicts to disclose.

Author Contributions

Retsuo Kawakami: Conceptualization (lead); Investigation (lead); Methodology (lead); Supervision (lead); Writing – original draft (lead). **Yuta Makino:** Formal analysis (supporting); Investigation (supporting); Methodology (supporting). **Shin-ichiro Yanagiya:** Formal analysis (supporting); Investigation (supporting); Methodology (supporting); Writing – original draft (supporting). **Akihiro Shirai:** Formal analysis (supporting); Investigation (supporting); Methodology (supporting); Writing – original draft (supporting). **Masahito Niibe:** Investigation (supporting); Writing – original draft (supporting). **Yoshitaka Nakano:** Formal

analysis (supporting); Investigation (supporting); Methodology (supporting); Writing – original draft (supporting).

DATA AVAILABILITY

The data that support the findings of this study are available from the corresponding author upon reasonable request.

REFERENCES

[1]I. Priyadarshini, A. Alkhayyat, A. J. Obaid, and R. Sharma, Cities **130**, 103970 (2022).
[2]Z. Yang, L. Zou, J. Xia, Y. Qiao, F. Bai, Q. Wang, and D. Cai, Ecol. Indic. **139**, 108892 (2022).
[3]N. Zamri, M. A. Pairan, W. N. A. W. Azman, S. S. Abas, L. Abdullah, S. Naim, Z. Tarmudi, and M. Gao, Proc. Comput. Sci. **204**, 172 (2022).
[4]S. Some, R. Mondal, D. Mitra, D. Jain, D. Verma, and S. Das, Energy Nexus **1**, 100008 (2021).
[5]G. Goshu, A. A. Koelmans, and J. J. M. de Klein, Environ. Pollut. **276**, 116693 (2021).
[6]D. S. de Almeida, L. D. Martins, and M. L. Aguiar, Chem. Eng. J. Adv. **11**, 100330 (2022).
[7]Z. Zhu *et al.*, Sci. Total Environ. **838**, 156364 (2022).
[8]Y. Zhang, R. Zhou, J. Chen, and N. Rangel-Buitrago, Ocean Coast. Manage. **219**, 106064 (2022).
[9]G. Baranyi *et al.*, Environ. Int. **169**, 107501 (2022).
[10]X. Shi, Y. Zheng, H. Cui, Y. Zhang, and M. Jiang, Ecotoxicol. Environ. Saf. **242**, 113893 (2022).
[11]D. Zhang, L. Chen, M. Xu, G. Feng, B. Zhang, H. Zhang, C. Yang, Q. Yu, and L. Wang, Appl. Surf. Sci. **605**, 154755 (2022).
[12]S. Khannyra, M. J. Mosquera, M. Addou, and M. L. A. Gil, Constr. Build. Mater. **313**, 125419 (2021).
[13]B. Balusamy, A. Senthamizhan, A. Celebioglu, and T. Uyar, J. Colloid Interface Sci. **593**, 162 (2021).
[14]H. Ji, Y. Cai, Z. Wang, G. Li, and T. An, Water Res. **221**, 118808 (2022).
[15]C. Liang *et al.*, Appl. Surf. Sci. **601**, 154144 (2022).
[16]R. Wang, J. Deng, P. Wu, Q. Ma, X. Dong, W. Yu, G. Liu, J. Wang, and L. Liu, J. Environ. Chem. Eng. **10**, 108173 (2022).
[17]H. Mohan, S. Vadivel, and S. Rajendran, Chemosphere **302**, 134827 (2022).
[18]H. Wang, Y. Yang, Z. Zhou, X. Li, J. Gao, R. Yu, J. Li, N. Wang, and H. Chang, Sep. Purif. Technol. **283**, 120192 (2022).
[19]S. Mittal, S. Garg, H. Bhandari, and V. Sharma, Inorg. Chem. Commun. **144**, 109834 (2022).
[20]Y. Zhang, H. Liu, F. Gao, X. Tan, Y. Cai, B. Hu, Q. Huang, M. Fang, and X. Wang, EnergyChem **4**, 100078 (2022).
[21]C. Cionti, E. Pargoletti, E. Falletta, C. L. Bianchi, D. Meroni, and G. Cappelletti, J. Environ. Chem. Eng. **10**, 108468 (2022).
[22]C. Thambiliyagodage, Environ. Nanotechnol. Monit. Manage. **18**, 100737 (2022).
[23]V. O. Odhiambo, T. L. Ba, Z. Konya, C. Cserhati, Z. Erdelyi, M. C. Naomi, and I. M. Szilagyi, Mater. Sci. Semicond. Process. **147**, 106699 (2022).
[24]Y. Yu *et al.*, Environ. Res. **214**, 114189 (2022).
[25]A. Dubsok, P. Khamdahsag, and S. Kittipongvises, J. Clean. Prod. **366**, 132928 (2022).
[26]S. Kumar *et al.*, Sci. Total Environ. **845**, 157221 (2022).
[27]N. D. Davlatshoevich, K. M. Ashur, B. A. Saidali, K. K. Tagoykulovich, A. Lyubchyk, and M. Ibrahim, Biointerface Res. Appl. Chem. **12**, 3836 (2022).
[28]D. Castilla-Caballero, O. Sadak, J. Martínez-Díaz, V. Martínez-Castro, J. Colina-Marquez, F. Machuca-Martínez, A. Hernandez-Ramirez, S. Vazquez-Rodriguez, and S. Gunasekaran, Mater. Sci. Semicond. Process. **149**, 106890 (2022).
[29]J. Bogdan, J. Zarzyńska, and J. Pławińska-Czarnak, Nanoscale Res. Lett. **10**, 309 (2015).
[30]Y. Jing *et al.*, Environ. Res. **203**, 111819 (2022).
[31]J. G. Mahy, R. G. Tilkin, S. Douven, and S. D. Lambert, Surf. Interfaces **17**, 100366 (2019).
[32]B. Li and N. Tang, Chem. Phys. Lett. **799**, 139636 (2022).
[33]Y. Hu, X. Song, S. Jiang, and C. Wei, Chem. Eng. J. **274**, 102 (2015).
[34]Y. Ammari, K. E. Atmani, L. Bay, I. Bakas, S. Qourzal, and I. A. Ichou, Mater. Today: Proc. **22**, 126 (2020).
[35]S.-S. Yong, J.-I. Lee, and D.-H. Kang, Food Microbiol. **109**, 104119 (2023).
[36]M. Xu, Y. Gao, E. M. Moreno, M. Kunst, M. Muhler, Y. Wang, H. Idriss, and C. Woll, Phys. Rev. Lett. **106**, 138301 (2011).
[37]T. Luttrell, S. Halpegamage, J. Tao, A. Kramer, E. Sutter, and M. Batzill, Sci. Rep. **4**, 4043 (2014).
[38]R. Kawakami *et al.*, Appl. Surf. Sci. **526**, 146684 (2020).
[39]R. Kawakami, Y. Mimoto, S. Yanagiya, A. Shirai, M. Niibe, Y. Nakano, and T. Mukai, Phys. Status Solidi (A) **218**, 2100536 (2021).
[40]L. Hou, M. Zhang, Z. Guan, Q. Li, and J. Yang, Appl. Surf. Sci. **428**, 640 (2018).
[41]D. Kuwana, Y. Komori, M. Nagatomo, and M. Inoue, J. Org. Chem. **87**, 730 (2022).
[42]R. Kawakami, M. Niibe, Y. Nakano, Y. Araki, Y. Yoshitani, C. Azuma, and T. Mukai, Vacuum **152**, 265 (2018).
[43]J. Saari, H. Ali-Löytty, K. Lahtonen, M. Hannula, L. Palmolahti, A. Tukiainen, and M. Valden, J. Phys. Chem. C **126**, 15357 (2022).
[44]J. C. C. Lo, S. W. R. Lee, X. Guo, and H. Zhao, Trans. Jpn. Inst. Electron. Packag. **9**, E16 (2016).
[45]S. Heinzmann, K.-D. Entian, and T. Stein, Appl. Microbiol. Biotechnol. **69**, 532 (2006).
[46]R. Kawakami, Y. Takao, A. Shirai, and T. Mukai, Biocontrol Sci. **27**, 217 (2022).
[47]M. T. Abdullah, L. M. Raoof, M. H. Hasan, A. N. Abd, and I. M. Mohammed, J. Phys.: Conf. Ser. **1999**, 012128 (2021).
[48]P. Makuta, M. Pacia, and W. Macyk, J. Phys. Chem. Lett. **9**, 6814 (2018).
[49]L. Harynski, A. Olejnik, K. Grochowska, and K. Siuzdak, Opt. Mater. **127**, 112205 (2022).
[50]S. A. Hamdan, I. M. Ibrahim, and I. M. Ali, J. Phys.: Conf. Ser. **2114**, 012025 (2021).
[51]B. L. Muhammad, N. V. Peterson, L. Kotsedi, and F. R. Cummings, Chem. Phys. **538**, 110922 (2020).
[52]B. Banerjee, V. Amoli, A. Maurya, A. K. Sinha, and A. Bhaumik, Nanoscale **7**, 10504 (2015).
[53]Y. Xu, S. Wu, P. Wan, J. Sun, and Z. D. Hood, RSC Adv. **7**, 32461 (2017).
[54]R. V. Nair, V. S. Gummaluri, M. V. Matham, and C. Vijayan, J. Phys. D: Appl. Phys. **55**, 313003 (2022).
[55]N. Serpone, J. Phys. Chem. B **110**, 24287–24293 (2006).
[56]X. Mettan *et al.*, Commun. Phys. **2**, 123 (2019).
[57]A. V. Bandura and J. D. Kubicki, J. Phys. Chem. B **107**, 11072 (2003).
[58]L. A. Garcia-Contreras, J. O. Flores-Flores, J. A. Arenas-Alatorre, and J. A. Chavez-Carvayar, J. Alloys. Compd. **923**, 166236 (2022).
[59]A. O. Bokuniaeva and A. S. Vorokh, J. Phys.: Conf. Ser. **1410**, 012057 (2019).
[60]S. Saravanan, M. Balamurugan, and T. Soga, Trans. Mater. Res. Soc. Jpn. **43**, 255 (2018).
[61]T. Ishigaki, Y. Nakada, N. Tarutani, T. Uchikoshi, Y. Tsujimoto, M. Isobe, H. Ogata, C. Zhang, and D. Hao, R. Soc. Open Sci. **7**, 191539 (2020).
[62]E. I. Vovk, A. V. Kalinkin, M. Y. Smirnov, I. O. Klembovskii, and V. I. Bukhtiyarov, J. Phys. Chem. C **121**, 17297 (2017).
[63]P. Bindra and A. Hazra, Vacuum **152**, 78 (2018).
[64]J. Lu, K. Liang, C. Xu, X. Wang, H. Ouyang, J. Huang, and L. Feng, Vacuum **163**, 292 (2019).
[65]K. Dong *et al.*, Chem Catal. **1**, 1437 (2021).
[66]X. Bi, G. Du, A. Kalam, D. Sun, Y. Yu, Q. Su, B. Xu, and A. G. Al-Sehemi, Chem. Eng. Sci. **234**, 116440 (2021).
[67]C.-Y. Wu, K.-J. Tu, J.-P. Deng, Y.-S. Lo, and C.-H. Wu, Materials **10**, 566 (2017).
[68]T. Kasuga, H. Kondo, and M. Nogami, J. Cryst. Growth **235**, 235 (2002).

[69]M. Setvin, U. Aschauer, P. Scheiber, Y.-F. Li, W. Hou, M. Schmid, A. Selloni, and U. Diebold, Science **341**, 988 (2013).
[70]J. Gao, J. Lyu, J. Li, J. Shao, Y. Wang, W. Ding, R. Cheng, S. Wang, and Z. He, Langmuir **34**, 7034 (2018).
[71]X. Pan, M.-Q. Yang, X. Fu, N. Zhang, and Y.-J. Xu, Nanoscale **5**, 3601 (2013).
[72]F. Guillemot, M. C. Porte, C. Labrugere, and C. Baquey, J. Colloid Interface Sci. **255**, 75 (2002).
[73]L. Kernazhitsky, V. Shymanovska, T. Gavrilko, V. Naumov, L. Fedorenko, V. Kshnyakin, and J. Baran, J. Lumin. **146**, 199 (2014).
[74]X. Zhong, T. Wang, Y. Li, Y. Yu, L. Chen, S. Liao, Y. Huang, and J. Long, RSC Adv. **11**, 23023 (2021).
[75]D. K. Pallotti, L. Passoni, P. Maddalena, F. Di Fonzo, and S. Lettieri, J. Phys. Chem. C **121**, 9011 (2017).
[76]N. D. Abazovic, M. I. Comor, M. D. Dramicanin, D. J. Jovanovic, S. P. Ahrenkiel, and J. M. Nedeljkovic, J. Phys. Chem. B **110**, 25366 (2006).
[77]A. Vazquez-Lopez, A. Cremades, and D. Maestre, Opt. Mater. Express **12**, 3090 (2022).
[78]S. Ma, M. E. Reish, Z. Zhang, I. Harrison, and J. T. Tates, J. Phys. Chem. C **121**, 1263 (2017).
[79]R. Kawakami, Y. Yoshitani, K. Mitani, M. Niibe, Y. Nakano, C. Azuma, and T. Mukai, Appl. Surf. Sci. **509**, 144910 (2020).
[80]A. R. Oromiehie, H. E. Dehaghani, K. Ansari, K. Karimi, Z. Rahmani, and S. Mirbagheri, J. Mater. Sci. Chem. Eng. **2**, 43 (2014).
[81]C. Karthik, S. Rajalakshmi, S. Thomas, and V. Thomas, Curr. Opin. Biomed. Eng. **26**, 100440 (2023).
[82]L. Y. Zang and H. P. Misra, J. Biol. Chem. **267**, 23601 (1992).